Uniaxial pulling and nano-scratching of a newly synthesized high entropy alloy

Cite as: APL Mater. 10, 111118 (2022); doi: 10.1063/5.0128135
Submitted: 26 September 2022 • Accepted: 1 November 2022 •
Published Online: 16 November 2022

Pengfei Fan,[1] Nirmal Kumar Katiyar,[2] Xiaowang Zhou,[3] and Saurav Goel[2,4,a)]

AFFILIATIONS

[1] Centre for Precision Manufacturing, DMEM, University of Strathclyde, Glasgow G1 1XQ, United Kingdom
[2] London South Bank University, 103 Borough Road, London SE1 0AA, United Kingdom
[3] Mechanics of Materials Department, Sandia National Laboratories, Livermore, California 94550, USA
[4] University of Petroleum and Energy Studies, Dehradun 248007, India

Note: This paper is part of the Special Topic on Design and Development of High Entropy Materials.
[a)] **Author to whom correspondence should be addressed:** GoeLs@Lsbu.ac.uk

ABSTRACT

Multicomponent alloys possessing nanocrystalline structure, often alluded to as Cantor alloys or high entropy alloys (HEAs), continue to attract the great attention of the research community. It has been suggested that about 64 elements in the periodic table can be mixed in various compositions to synthesize as many as ~10^8 different types of HEA alloys. Nanomechanics of HEAs combining experimental and atomic simulations are rather scarce in the literature, which was a major motivation behind this work. In this spirit, a novel high-entropy alloy ($Ni_{25}Cu_{18.75}Fe_{25}Co_{25}Al_{6.25}$) was synthesized using the arc melting method, which followed a joint simulation and experimental effort to investigate dislocation-mediated plastic mechanisms leading to side flow, pileup, and crystal defects formed in the sub-surface of the HEA during and after the scratch process. The major types of crystal defects associated with the plastic deformation of the crystalline face-centered cubic structure of HEA were 2,3,4-hcp layered such as defect coordination structures, coherent $\sum 3$ twin boundary, and $\sum 11$ fault or tilt boundary, in combination with Stair rods, Hirth locks, Frank partials, and Lomer–Cottrell locks. Moreover, 1/6 <112> Shockley, with exceptionally larger dislocation loops, was seen to be the transporter of stacking faults deeper into the substrate than the location of the applied cutting load. The (100) orientation showed the highest value for the kinetic coefficient of friction but the least amount of cutting stress and cutting temperature during HEA deformation, suggesting that this orientation is better than the other orientations for improved contact-mode manufacturing.

I. INTRODUCTION

High entropy alloys (HEAs) are multicomponent alloys comprising at least five elements from the periodic table, with each element within a concentration range of 5%–35%. HEAs were formally reported by Yeh *et al.*[1] and Cantor *et al.*[2] in 2004, although Cantor developed them long ago in the 1990s through a student project and left academia to join the industry, and it is in his honor that HEAs are also referred to as Cantor alloys. HEAs are endowed with exceptional properties compared to conventional solid–solid solution alloys, which has led to an accelerated global effort in exploring the potentials of HEAs as structural materials,[3] functional materials,[4] smart materials, and sensors[5] as well as biocompatible materials,[6,7] to name a few. Many of these aspects of HEAs are discussed in a recent review paper written by the authors, focusing on the use of machine learning in predicting the crystal structure of HEA.[8]

HEAs are now being explored in various engineering applications, including superb ultra-high temperature materials for exhaust nozzle,[9] combustion chambers,[10] compressors,[11] gas turbine case applications in the aerospace engine,[12] and excellent superconductor magnetic materials to create magnets powerful enough to levitate trains with low-loss transmission of electricity.[13] Additionally, the exceptional abrasive resistance of HEAs is significant for the use of moving components in industrial applications, e.g., bearings and gears. The higher strength and better deformation resistance characteristics of HEAs are significant for all these applications. Moreover, these applications are governed by the nanotribology of

HEA, hitherto poorly understood. This is acutely important, given the responsible use of mined materials, as some of the constituent metals required to synthesize HEAs are at critical import risk, which is often referred to as critical raw materials (CRMs).[14]

Numerical solvers, such as *ab initio* and finite element methods,[15] are unsuitable for studying the tribology of HEA due to the length scale problem and the lack of appropriate material constitutive models. In this sense, molecular dynamics (MD)[16,17] is an appropriate tool to understand plasticity mechanisms in HEA. Combining this simulation-led discovery with an experimental campaign of contact loading study on HEA using nanoscratching[18] was the key highlight of this work.

Recent works have reported some aspects of plastic deformation in HEAs, such as $Al_{0.1}CoCrFeNi$,[19,20] FeCoCrNiCu,[21] AlCrCuFeNi,[22] and CrMnFeCoNi,[23,24] by using the classical EAM potential function in MD simulations in conjunction with experimental methods such as *in situ* transmission electron microscope (TEM) uniaxial stress.[25,26] The uniaxial stress situation differs from the deviatoric stress condition often witnessed in contact conditions, such as scratching, and since the studies in this area are scarce, this nanoscratching investigation on the newly synthesized HEA is novel.

A study such as this one is necessary to answer open questions to address concerns such as (i) the supercell of HEA developed using the special quasi-random structure (SQS) method does not introduce large prediction errors, (ii) the EAM potential energy function available to simulate the HEA alloy can still be used reliably for performing nanomechanical studies, and (iii) whether a face-centered cubic (FCC) structure of HEA deforms akin to normal FCC metals, such as copper and aluminum, or shows distinct deformation mechanisms. In pursuit of the answers to these questions, a novel high entropy alloy ($Ni_{25}Cu_{18.75}Fe_{25}Co_{25}Al_{6.25}$) was first prepared in the lab, and experiments were then performed alongside the MD simulations to explain the nanomechanical behavior of this unique FCC HEA.

II. EXPERIMENTAL AND SIMULATION SETUP

A. Experimental synthesis and characterization of $Ni_{25}Cu_{18.75}Fe_{25}Co_{25}Al_{6.25}$ alloy

The Ni, Cu, Fe, Co, and Al metal buttons were purchased from Thermofisher Scientific® with 99.99% purity. All metal buttons were melted together by arc melting in an inert gas (Ar) environment. The melted matrix was solidified, remelted, and resolidified multiple times to ensure homogeneity. The mixing ratio was chosen selectively to obtain $Ni_{25}Cu_{18.75}Fe_{25}Co_{25}Al_{6.25}$. The HEA button was vacuum sealed in a quartz tube, homogenized at 1000 °C for 10 hours, and then quenched into the water to freeze the high-temperature phase. The sample thus obtained was analyzed using x-ray diffraction analysis (see Fig. 1), which confirmed that the alloy stabilized into a single-phase FCC alloy.

B. Nano-scratching experiments

In this paper, an instrumented nano-scratching apparatus from Micromaterials Limited (Platform 5, NanoTest Vantage, based at London South Bank University, UK) was used to carry out the nanomechanical testing (see Fig. 2). The loading mechanism comprises a pendulum that rotates around a pivot and is loaded electromagnetically. The test sample was mounted vertically, and the test probe displacement was measured with a parallel plate capacitor with sub-nm resolution.

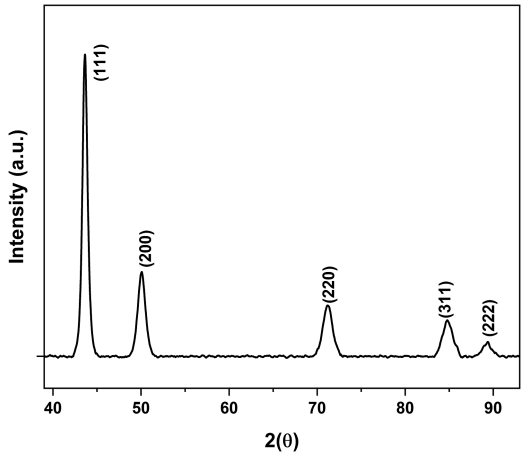

FIG. 1. X-ray diffraction analysis of the newly synthesized high-entropy alloy $Ni_{25}Cu_{18.75}Fe_{25}Co_{25}Al_{6.25}$.

During nano-scratching, a spheroconical diamond indenter with an end radius of 5 μm and an included angle of 90° was used, as shown in Fig. 3(a). As shown in Figs. 3(a) and 3(b), the load function in a load-control mode (with a low load head) at room temperature (~20 °C) was used to perform the nano-scratching experiments. With this load function, the tip created a total scratch length of 480 μm such that the initial 250 μm length of scratch at the start used a ramping load of 0–500 mN and the 230 μm length of remaining scratch was performed at a constant load of 500 mN.

C. MD simulation model development of the high-entropy alloy $Ni_{25}Cu_{18.75}Fe_{25}Co_{25}Al_{6.25}$

The atomic model construction of HEA is a complex process. The two schemes available to perform this task are cluster expansion and special quasi-random structures (SQS). Of these methods, the SQS method is more popular and is implemented in software such as Atomsk.[27] Once a structure of HEA, either in the form of a cylindrical wire (for nano-tensile tests), or a cubic block (for nano-scratching tests), is made, it can be fed to software, such as LAMMPS (a large-scale atomic/molecular massively parallel simulator),[28] to perform the MD simulations. The visualization of the modeling data were performed using the Open Visualization Tool (OVITO). In OVITO, an automated "dislocation extraction algorithm" (DXA) implementation facilitates *in situ* analysis of various dislocations and crystal defects, which provides a rapid assessment of the MD data.[18,29,30]

1. MD model parameters

The MD model comprises two types of geometries, namely, a cylindrical wire and a cubical block containing HEA atoms. Two types of cylindrical wires with the same aspect ratio of 0.66 were constructed: one short wire with a diameter of 7.2 nm and a length

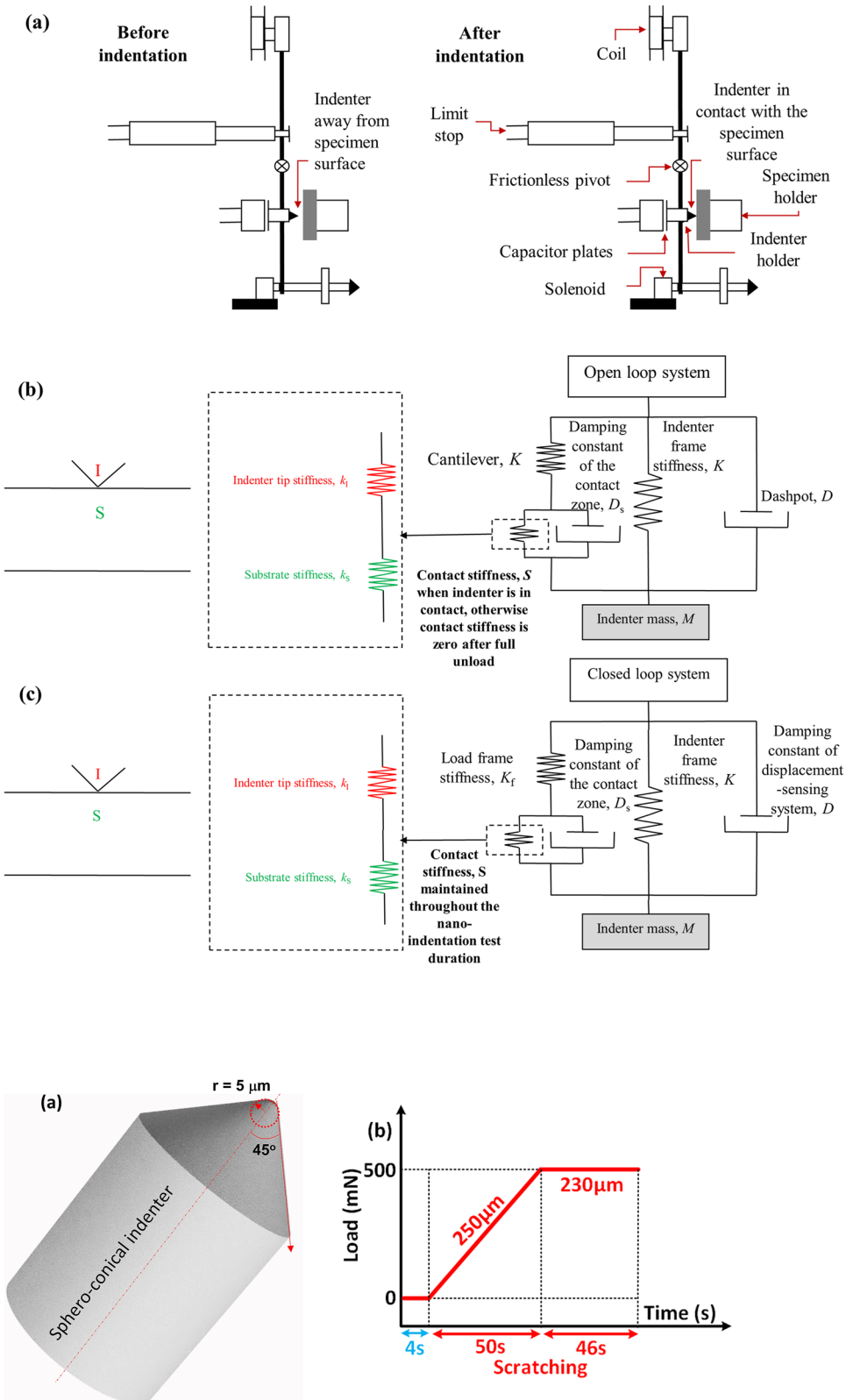

FIG. 2. Indentation contact model: (a) schematic before and after indentation (adapted from Micro Materials Ltd. and from Faisal *et al.*, Surf. Coatings Technol. **242**, 42–53 (2014). Copyright 2014 Elsevier[18]), (b) open loop loading/unloading mechanism for nano-indentation test, and (c) closed loop loading/unloading mechanism used previously (I: indenter and S: substrate).

FIG. 3. (a) Schematic of a spheroconical indenter tip and (b) nano-scratching load profile.

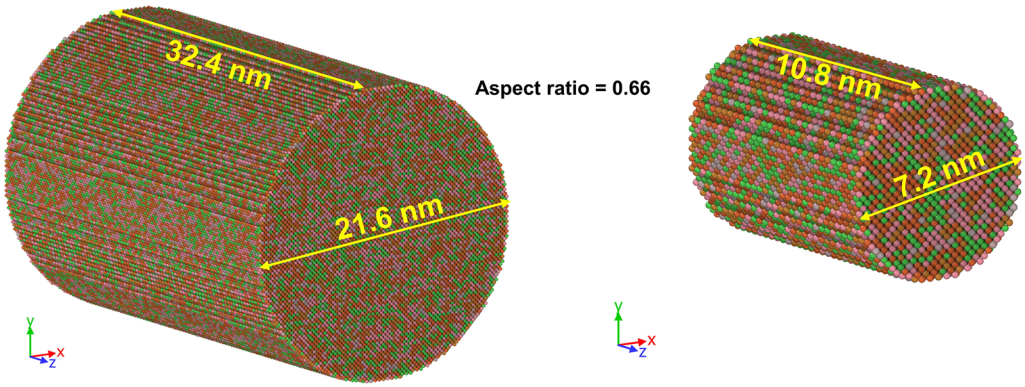

FIG. 4. Illustration of the nanowire geometry of the $Ni_{25}Cu_{18.75}Fe_{25}Co_{25}Al_{6.25}$ alloy.

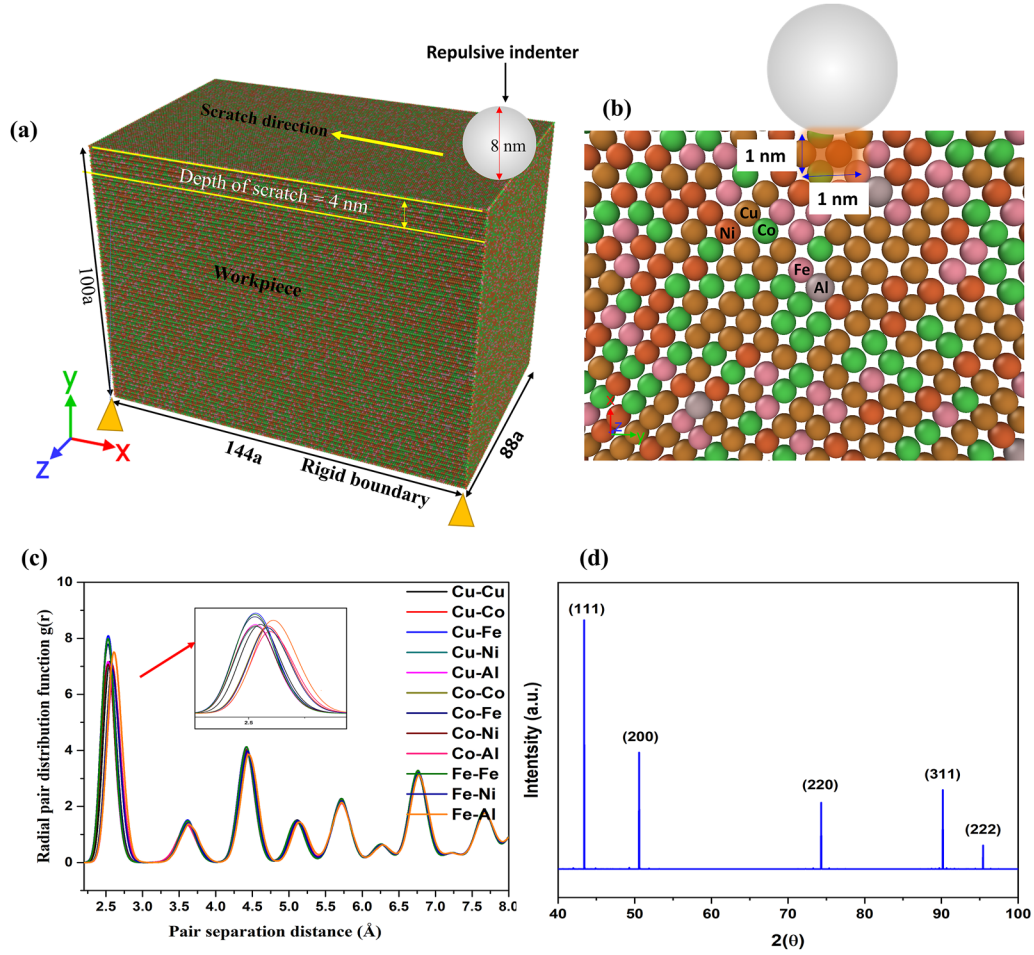

FIG. 5. Schematic diagram of the (a) scratch simulation model with lattice constant ***a*** = 3.615 Å, (b) ($1 \times 1 \times 1$ nm^3) volume of atoms was considered for computation of scalar stress and temperature calculations acting in the scratched zone (only 2D representation of 3D volume in XY plane is shown here), (c) radial distribution function showing all individual peaks of atoms in the HEA workpiece, and (d) simulated x-ray diffraction pattern of the HEA workpiece in one orientation revealing a crystalline FCC structure. All three orientations of HEA showed the same XRD.

TABLE I. Detailed parameters used for the MD simulation of the $Ni_{25}Cu_{18.75}Fe_{25}Co_{25}Al_{6.25}$ HEA alloy.

Dimensions of the HEA workpiece	144a × 100a × 88a, where 'a' is 3.615 Å, which is the equilibrium lattice parameter of the $Ni_{25}Cu_{18.75}Fe_{25}Co_{25}Al_{6.25}$ at 300 K
Initial distance between the indenter and workpiece surface	0.2 nm
Depth of scratch	4 nm
Scratch velocity	50 m/s
Scratch distance	25 nm
Spherical tool diameter	8 nm
Timestep for MD calculation	1 fs
Boundary conditions	sm s p in the X, Y, and Z directions, respectively
Workpiece setup for scratching simulations	Case 1: <100> (010) Case 2: <−110> (110) Case 3: <−110> (111)
Ensemble used in the simulation	NVE at 300 K

of 10.8 nm, and one large wire with a diameter of 21.6 nm and a length of 32.4 nm. The nanowires were built in three orientations: (i) the (111) plane oriented on the *z* axis; (ii) the (110) plane oriented on the *z* axis; and (iii) the (100) plane oriented on the *z* axis (see Fig. 4).

These wires were subjected to a nanoscale tensile test by pulling them in the *z* direction. A periodic boundary condition was prescribed in the *z* direction, and a shrink-wrapped condition was used in the *X* and *Y* directions. The model was thermally equilibrated at 300 K, and then a strain rate of 5×10^8 s^{-1} was used to perform the tensile testing.

As for the scratch test, a work piece of size 51.42 × 36.05 × 31.81 nm^3 was modeled, containing 4 998 400 (five types) total atoms of high-entropy alloys [see Figs. 5(a)–5(c)]. The bottom part of this work piece was made rigid by prescribing a fixed boundary condition to hold the workpiece in place during scratching, and a small thermostatic layer was added next to the rigid layer to allow smooth heat dissipation from the workpiece during scratching. As for the indenter, a strong repulsive[31] and rigid-type spherical indenter of 8 nm diameter was modeled. This assumption was necessary due to the lack of a potential energy function parameterized for interactions between carbon atoms (tool) and

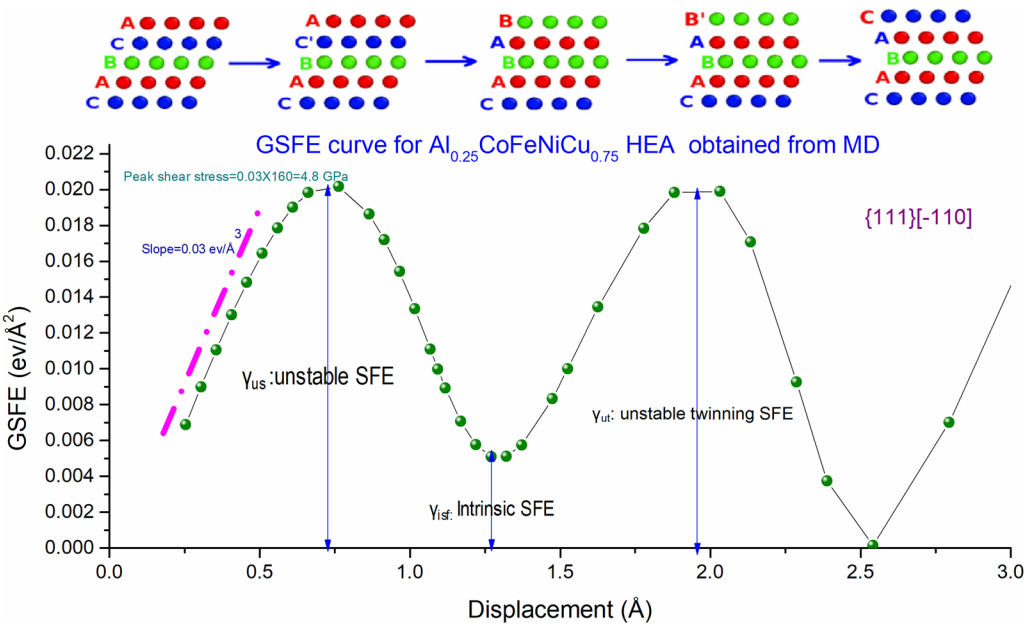

FIG. 6. Generalized stacking fault energy of $Ni_{25}Cu_{18.75}Fe_{25}Co_{25}Al_{6.25}$ on the shuffle set.

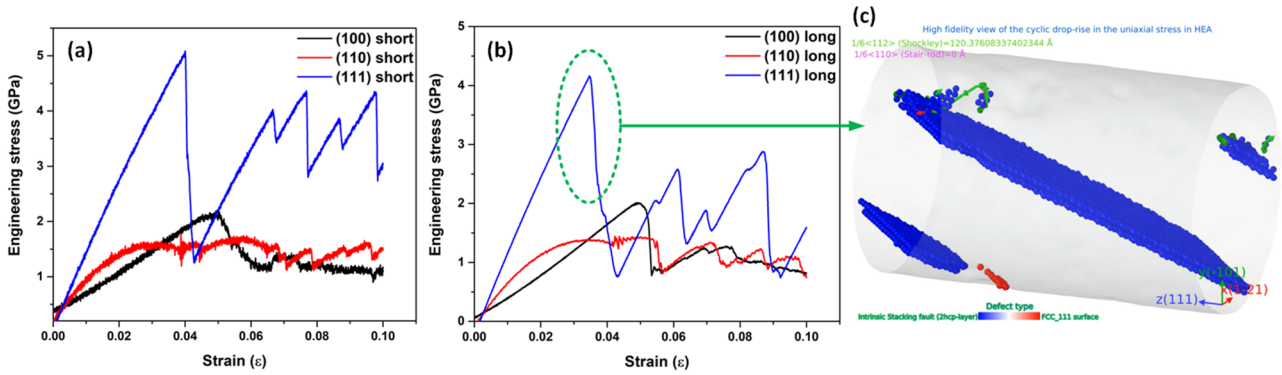

FIG. 7. Stress–strain curves for (a) short and (b) long wires of HEA obtained from the MD simulations for all three crystal orientations, namely [111], [110], and [100]. Higher yield stress for the shorter wire than the longer wire signifies the size effect. (c) Crystal defect analysis reveals periodic formation of slip bands (in blue), accounting for the periodic drops in the stress–strain curves.

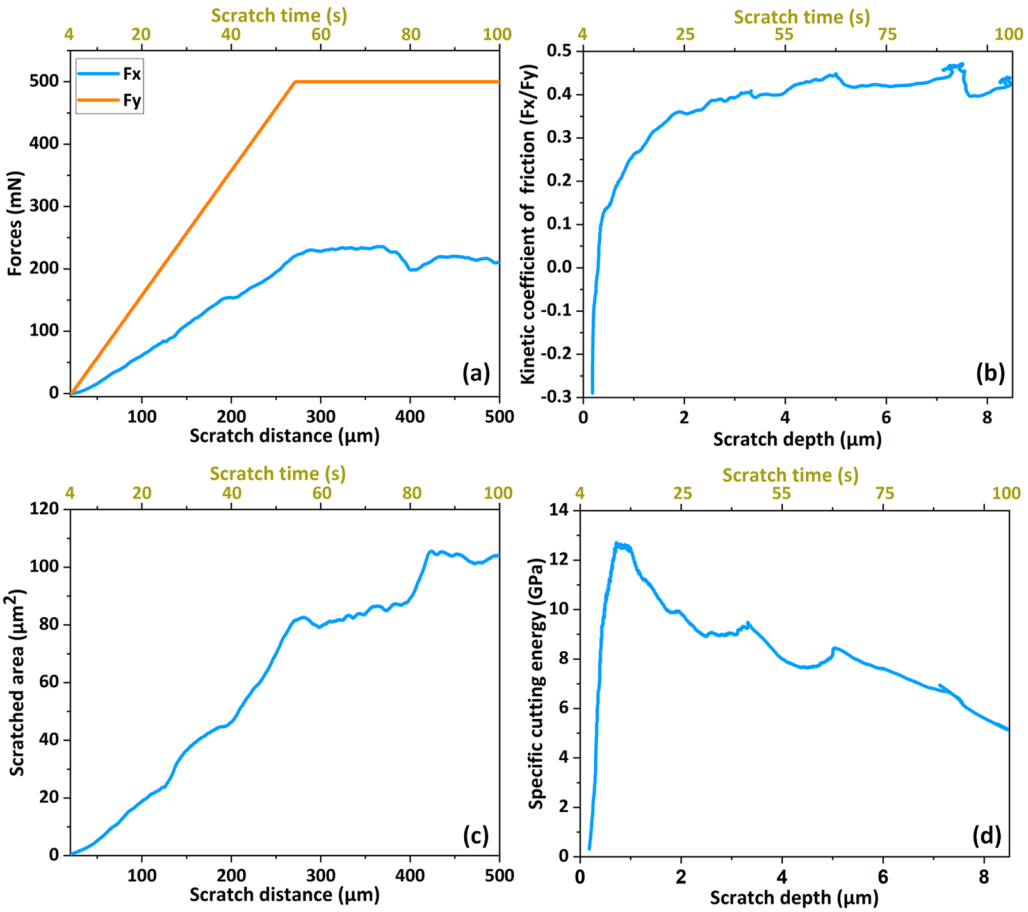

FIG. 8. Nano-scratching experiments performed on the $Ni_{25}Cu_{18.75}Fe_{25}Co_{25}Al_{6.25}$ high-entropy alloy using a spheroconical diamond indenter showing (a) evolution of friction force (*Fx*) and normal force (*Fy*) as a function of scratch distance, (b) the evolution of the kinetic coefficient of friction (*Fx*/*Fy*) as a function of scratch depth, (c) variation in the scratched area with scratch distance, and (d) variation of the specific cutting energy as a function of scratch depth.

workpiece (HEA atoms). The indenter was given a velocity at the beginning of the simulation to travel a certain distance into the workpiece using LAMMPS NVE dynamics. During this motion, each atom in the indented material interacts with the idealized indenter to experience a force of magnitude $F(r) = K(r-R)^2$, where K is the force constant (1 KeV/Å^3), R is the radius of the spherical indenter, and r is the distance of an atom of the work piece from the center of the spherical indenter. This implies that F(r) remains repulsive if R > r or becomes zero otherwise. Further parameters used to perform the scratch simulation are shown in Table I.

2. Verification of the HEA model developed using the SQS method

After the initial model development following the SQS method, the radial distribution function was estimated [see Fig. 5(c)]. The radial distribution function (RDF) signifies that the workpiece was a long-range, crystalline-ordered structure. Simulated x-ray diffraction (XRD) in LAMMPS was also obtained for this structure to gather experimentally comparable data as evidence to prove that the modeled HEA had the same crystal structure that was synthesized experimentally. This becomes particularly clear from comparing Fig. 5(d) with Fig. 1, which is a direct comparison between experimental and simulated XRD of the high-entropy alloy synthesized for the first time in this work.

3. Potential energy function and stacking fault energy assessment

An EAM potential developed by Zhou *et al.*[32] at Sandia Labs was used to describe the interactions between the five atoms of Ni, Cu, Fe, Co, and Al that make up the HEA. Since the stacking fault energy is important to mechanical deformation, it was appropriate to assess the generalized stacking fault energy (GSFE) on the Shuffle plane (111) <−110> of the high-entropy alloy $Ni_{25}Cu_{18.75}Fe_{25}Co_{25}Al_{6.25}$. Generalized stacking fault energy was first proposed by Vitek[33] in 1966 and recently has been proven as a critical criterion for dislocation slip, twinning, and plastic deformation mechanisms.[34] GSFE can be computed as[35]

$$\gamma(d) = \frac{E(d) - E_0}{A}, \tag{1}$$

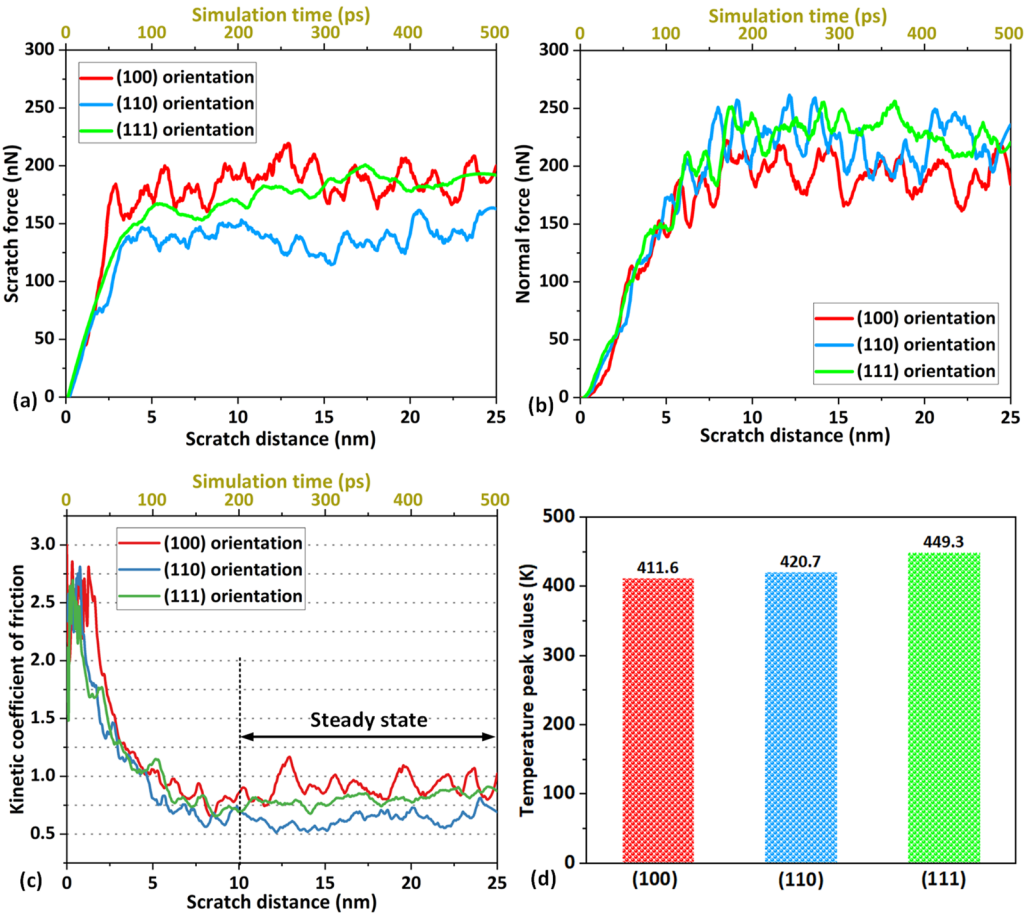

FIG. 9. Variation of (a) scratch force (*Fx*) and (b) normal force (*Fy*) on all three crystallographic orientations, (c) evolution of the kinetic coefficient of friction on all orientations, and (d) temperature peak values in the scratch zone of HEA in all three different orientations obtained from MD simulations.

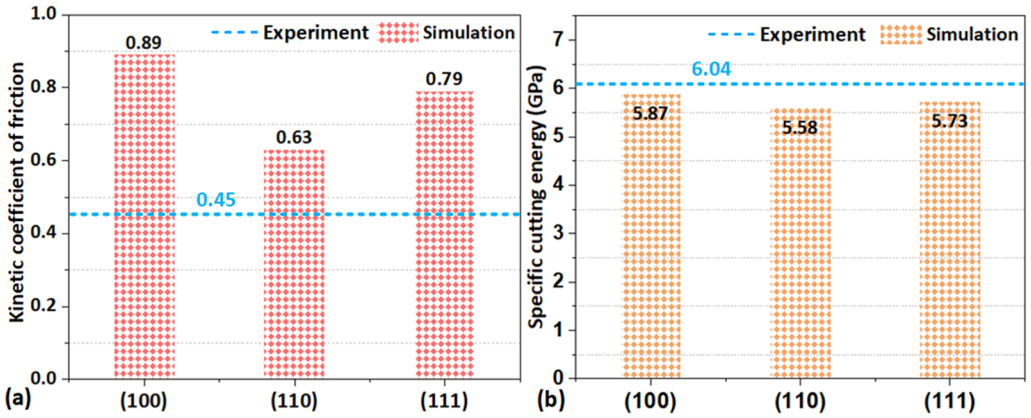

FIG. 10. Comparison of the MD simulation and experimental results in (a) kinetic coefficient of friction and (b) specific cutting energy.

where A represents the defect area, E_0 means the energy of a perfect crystal structure, and $E(d)$ is the total energy of the deformed crystal.

Intrinsic stacking fault is a planar defect that is a common occurrence in face-centered cubic (FCC) metals during their deformation. The natural stacking arrangement for FCC metals on the closed-packed (111) plane is ABCABCAB. . ., but if an intrinsic stacking fault is introduced, the stacking arrangement changes to ABCBCABC. . .. It is as if one closed plane, A in this case, has been removed, disrupting the otherwise perfect stacking. Since the modeled high entropy alloy resides in an FCC phase, it was considered appropriate to obtain the generalized stacking fault energy for this alloy, which is shown in Fig. 6. The unstable stacking fault energy (γ_{us}), which is the first maximum point on the GSFE curve based on Rice's brittle-to-ductile transition model,[36] was found to be 0.02 eV/Å^2. γ_{us} represents the energy barrier for defect nucleation. The second maximum point of GSFE is the unstable twinning fault energy (γ_{ut}). The intrinsic stacking fault energy γ_{isf} was estimated to be about 0.005 eV/Å^2. From Fig. 6, it was seen that the GSFE trend for HEA possessed some similarity with other FCC metals, such as copper, as reported previously by other researchers. The slope of GSFE with respect to the displaced atoms obtained from Fig. 6 suggested that about 4.8 GPa shear stress will cause the first instability in the structure, paving the way for the defect nucleation to occur.

III. RESULTS AND DISCUSSION

A. MD simulation of the uniaxial tensile test of the HEA nanowires

Figures 7(a) and 7(b) show the engineering stress–strain curves for the two wires of HEA simulated using MD. The highest yield stresses occur during the [111] loading, yielding about 5 GPa and 4 GPa for the short and long wires, respectively. The lowest yield stresses occur during the [110] loading. The tensile stress–strain curves of the short and long nanowires showed close similarity in both magnitude and trend; however, frequent drops in the stresses (almost periodically) were noticedthis was unique in the HEA nanowire compared to other FCC nanowires that have been previously simulated by other researchers. This suggests frequent emission and propagation of dislocations.

A video was made from the simulated data (provided as complimentary data) to better understand the emission and propagation of the defects during tensile pulling. It was noticed that as soon as the HEA wire was subjected to tensile stress, an intrinsic stacking fault with a two-hexagonal close-packed (HCP) layer like coordination structure emitted from the surface of the wire, traveling at an angle inside the wire until reaching the circumference at the other end of the wire, as shown in Fig. 7(c). A video of the tensile deformation showing the emission of dislocation from one end terminating at

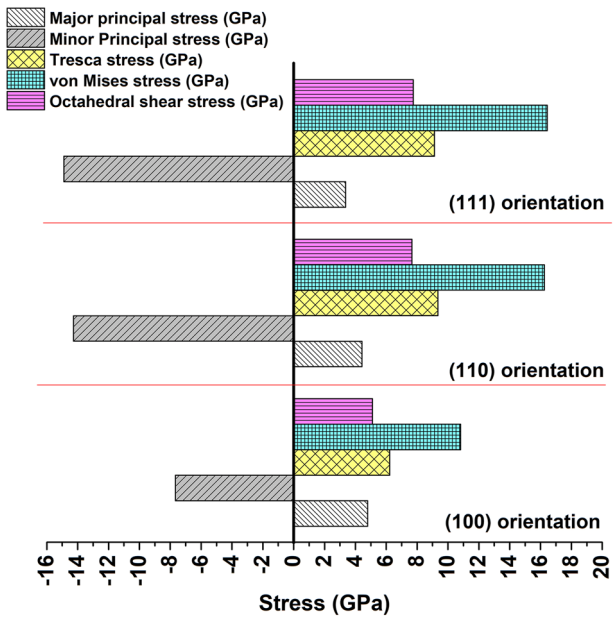

FIG. 11. Peak average stresses during scratching processes obtained from MD simulations for three crystallographic orientations.

the other end of the nanowire of HEA is provided as supplementary information. We suggest that the emission of the intrinsic stacking faults relieves the stress intermittently, causing the cyclic drop in the uniaxial stress–strain curves.

B. Experimental measure of scratch force, kinetic coefficient of friction, and specific cutting energy

The scratch experiments were carried out using a ramp loading function on the polycrystalline HEA prepared in the lab, as discussed previously. The experimental scratching results are plotted in Fig. 8, showing the measurement of scratched forces (friction and normal forces), evolution of the kinetic coefficient of friction, evolution of the scratched area, and specific cutting energy (work done by the scratching tool in removing unit volume of material). The normal force was seen to vary from 0 to 500 mN, and it stayed at this magnitude during the course of nano-scratching. The maximum scratch depth at 500 mN force was of the order of 8 μm, and the friction force approached a value of about 225 mN. During steady-state nano-scratching, the kinetic coefficient of friction, which is the ratio of friction and normal forces (Fx/Fy), showed a value close to 0.45.

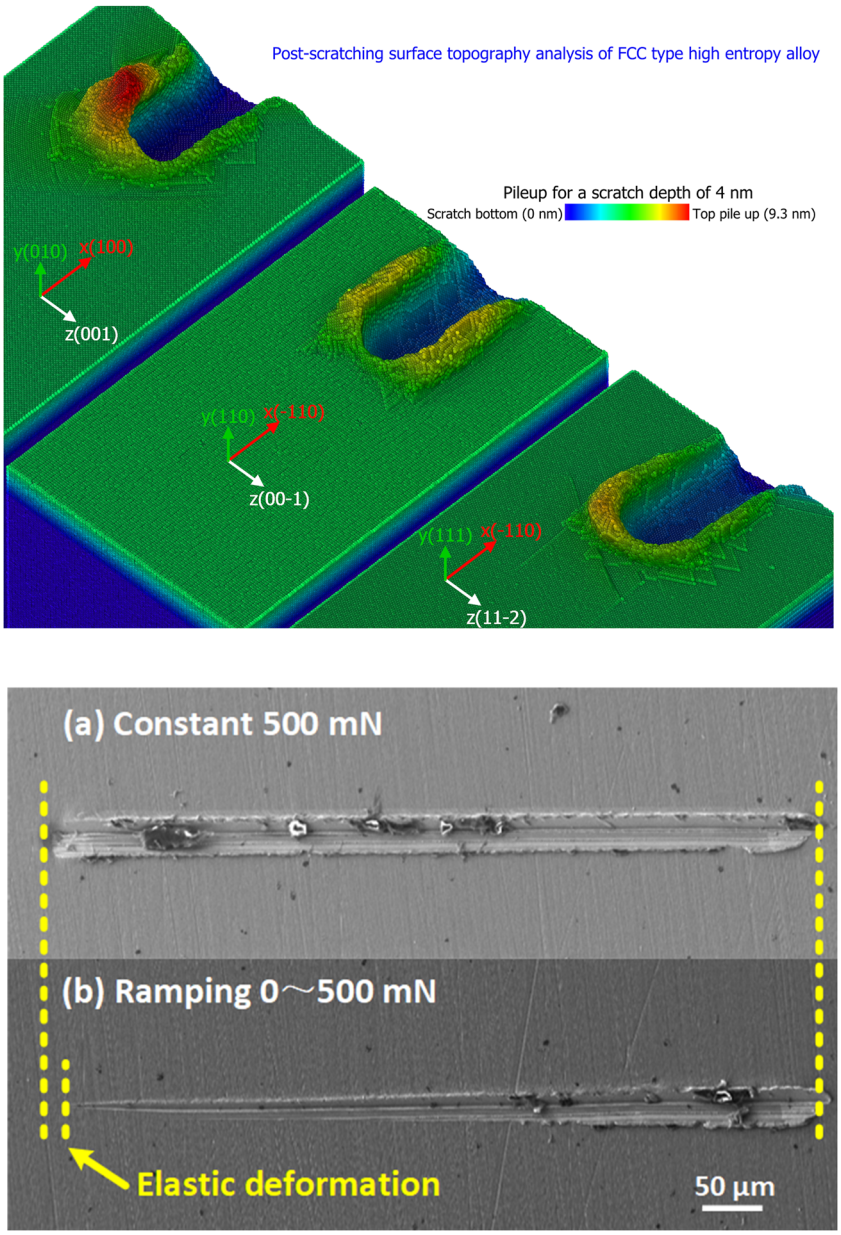

FIG. 12. Topography of the HEA workpiece after scratch (i) obtained from MD simulation using a spherical indenter under depth- or velocity-controlled scratching and (ii) nanoscratching experiments with a spheroconical indenter (a) under a constant load of 500 mN and (b) under a ramped load from 0 to 500 mN as per the load function shown earlier in Fig. 3(b).

C. MD simulation estimates of scratch force, kinetic coefficient of friction, stress, and specific cutting energy

Figures 9(a) and 9(b) show the variation in the scratching forces (along the direction of the scratch and normal to the surface) in all three crystallographic orientations obtained from the MD simulations. In the initial state of scratching, the material initially experiences pure compression, and at this stage, the scratch force increases monotonically. After the material undergoes sufficient compression, the material removal process begins as soon as the compression is dominated by shear. In this state, the combined action of shear and compression paves the way for the material to flow plastically in the solid state. During this stage, steady-state scratching leads to a saturated regime of forces, which is an ideal regime to calculate and estimate the average scratch forces and kinetic coefficient of friction. The ratio of the two scratch forces, i.e., F_x (friction force) and F_y (normal force), is also referred to as the kinetic coefficient of friction, which is an important measure for the assessment of the tribology of the surface. From the MD data of the scratch forces, the kinetic coefficient of friction obtained from the simulation for the different orientations was seen to vary from 0.6 to 0.9, while it was minimum for the (110) orientation and maximum for the (100) orientation [See Fig. 9(c)]. The value of the experimentally measured coefficient of friction was close to 0.45. The corresponding temperature peak values in the stressed zone are shown in Fig. 9(d). The (111) orientation was seen to be hotter than the (100) and the (110) orientations.

Figure 10 provides a comparison between the simulations and the experiments by way of measuring the kinetic coefficient of friction and the specific cutting energy. The specific cutting energy obtained from MD was found to be maximum for the [100] orientation and minimum for the [110] orientation. The experimental specific cutting energy was estimated to be 6.04 GPa, as illustrated in Fig. 10(b), close to the MD values. The average kinetic coefficient of friction from simulations deviates relatively from the experimental value, as shown in Fig. 10(a). This phenomenon was also noticed by the authors of this paper during the cutting of single-crystal GaAs.[30] Note that the differences in the kinetic coefficient of friction can have numerous origins: (i) the specimen used in the experiments was polycrystalline, whereas the simulations were performed on a single crystal material, (ii) the length scales used in experiments and simulations were dramatically different, and (iii) the specimen used in experiments may contain surface oxides and contamination, which do not exist in simulations. In view of these, we consider specific cutting energy as a more appropriate measure to compare experiments and simulations, especially because this property is independent of the geometry of the scratching tool used in simulations and experiments.

From the scalar measure of the stress tensor in the scratch zone, we estimated the peak average of Tresca stress, von Mizes stress, principal stresses (minor and major), and octahedral shear stresses,

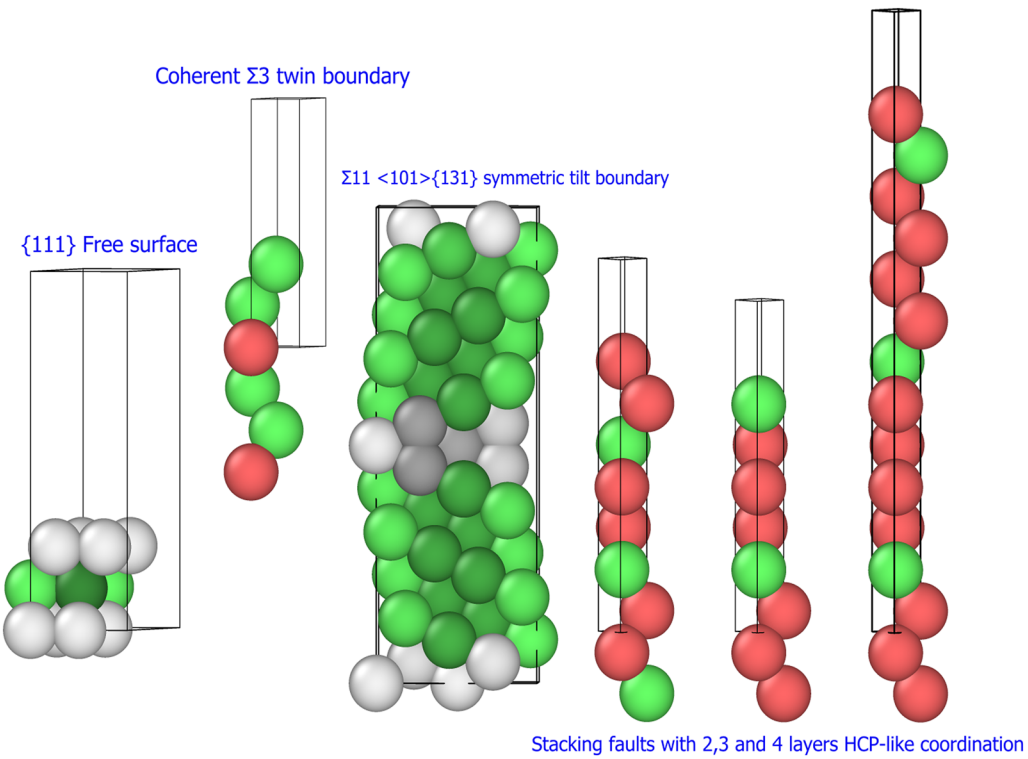

FIG. 13. Defect template used to analyze crystal analysis.

as shown in Fig. 11. The relevant formulas for calculation are provided in the supplementary material. Except for the major principal stress criterion, all criteria seem to indicate that the [100] orientation deforms at a lower stress than the other two orientations. The von Mizes stress in the scratched zone of the [100] orientation was about 10.5 GPa, while for the other orientations, it was of the order of 16 GPa. The octahedral shear stress on the [100] orientation was close to 5 GPa, which was close to the value of shear stress (4.8 GPa) obtained from the GSFE curve.

D. Side flow, pileup, and crystal defects seen during nano-scratching MD simulations of HEA

1. Side flow and pileup

The topography of HEA scratches obtained from MD simulations is shown in Fig. 12. One can see a pileup of HEA atoms as well as the side flow on both sides of the nanogrooves on all crystallographic planes. The (010) crystal orientation showed the maximum height of the pileup, whereas the (111) orientation showed the maximum extent of dislocation activities in front of the scratching tool, which is evident on the top part of the scratched surface. The post-scratching surface topography obtained from simulations for all three orientations suggests that HEA exhibits strong anisotropic effects akin to other commonly known FCC metals such as copper and aluminum. In the case of (110), most HEA atoms pile up on both sides of the nanogroove and reach evenly up to 3.5 nm above the surface. In terms of material removal, it can be said that the material pileup for the (010) orientation occurred at an angle in a south-west direction from the front of the cutter, whereas for the (110) orientation, the pileup was equally divided on both sides of the scratching tool. The (111) orientation showed a somewhat uniform pileup on all sides of the surface, with a slightly higher amount in the front of the cutter as seen in the (010) orientation. On the experimental side, two nanoscratch images obtained from the SEM are provided, which were under a constant load of 500 mN and a ramp load from 0 to 500 mN, as per the load function shown earlier in Fig. 3(b). From this simple comparison, it is easier to see that for about 10–15 μm, the HEA showed full elastic recovery during scratching for the applied load conditions. HEA can be seen to flow on both sides of the scratching tool, albeit the extent of side flow can be seen to increase significantly from Fig. 12 (ii) (b) beyond a scratch length of 220 μm.

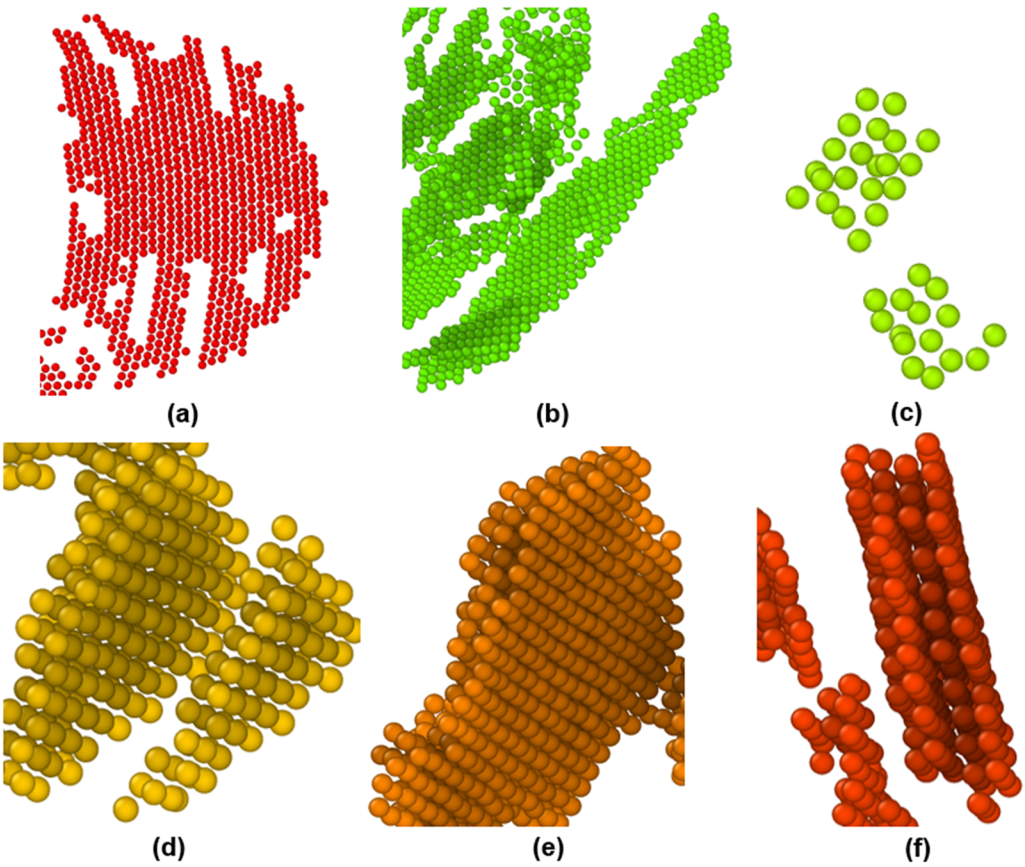

FIG. 14. Details of various types of crystal defects extracted from the MD simulation. (a) {111} free surface atoms, (b) Σ3 grain boundaries, (c) Σ11 fault or tilt boundaries, (d) 2 HCP layers, (e) 3 HCP layers, and (f) 4 HCP layers.

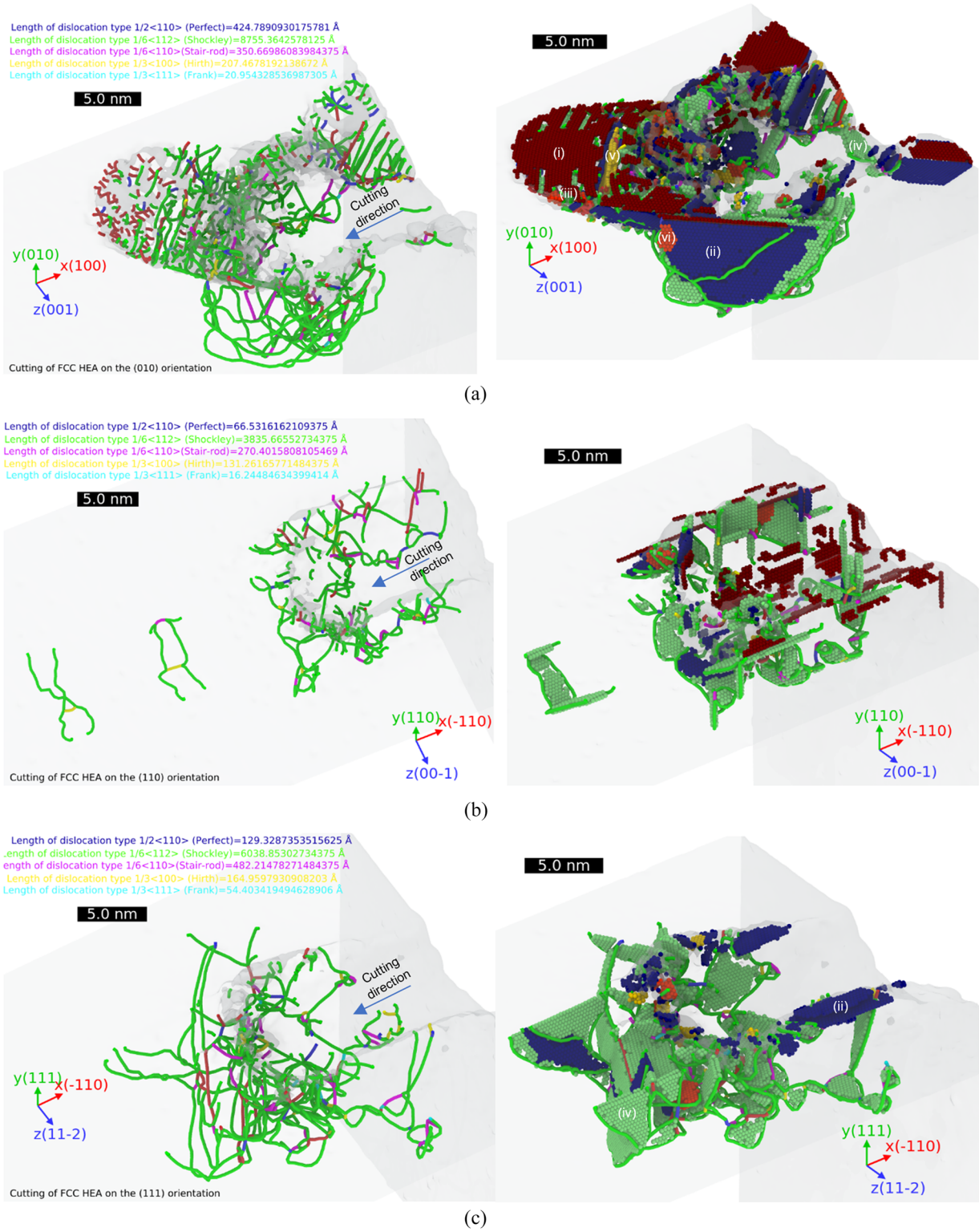

FIG. 15. Defect structures observed in HEA for different orientations. (i): {111} free surface atoms, (ii): ∑3 coherent twin boundary, (iii): ∑11 <101> {131} tilt boundary, (iv), (v), and (vi): HCP phase with 2, 3, or 4 layer thickness. (a) Defect structures in HEA during nanoscratching on the (100) orientation, (b) defect structures in HEA during nanoscratching on the (110) orientation, and (c) defect structures in HEA during nanoscratching on the (111) orientation.

2. Planar defects and dislocation types observed in the HEA scratches during MD simulations

Planar defects near the scratched surface and the sub-surface govern the quality of cutting as well as the plasticity mechanisms by which most of the material is transported during the material removal process. As for the FCC material, the commonly known planar defect templates for deformation are shown in Fig. 13. These include the {111} free surface, the coherent ∑3 twin boundary, the ∑11 <101> {131} symmetric tilt boundary, and the HCP phase with either 2, 3, or 4 layers of thickness. These defects were seen in HEA to not only be limited to the scratched area but also along the side of the scratch, where the stress was not sufficient to cause the material to flow. In some cases, the side flow or piled-up structures also showed additional types of faults. The other forms of defects observed were associated with intrinsic and extrinsic stacking faults, and the extent of these varied with the orientation of the HEA substrate. These planar defects result from the propagation of partial dislocations. Figure 13 highlights the portion of scratched material where these defect types were observed in the simulations. A more detailed visualization of these defects, directly extracted from the simulated nanoscratched specimens, is shown in Figs. 14 and 15.

As illustrated in Figs. 14 and 15, the crystal defects in HEA consist of {111} free surface atoms, ∑3 coherent twin boundaries, ∑11 <101> {131} tilt boundaries, and HCP-like coordination with 2, 3, or 4 layer thickness. Regardless of the orientation scratched, five different dislocation types were seen, namely, 1/2 <110> perfect dislocations, 1/6 <112> Shockley dislocation, 1/6 <110> Stair-rod dislocation, 1/3 <100> Hirth dislocation, and 1/3 <111> Frank dislocation.

Specifically, dislocations for the (100) orientation were mostly of 1/2 <110> perfect (42.48 nm), 1/6 <112> Shockley (875.54 nm), 1/6 <110> stair rod (35 nm), and 1/3 <100> Hirth (20.75 nm). The dislocations for the (110) orientations were perfect (6.6 nm), 1/6 <112> Shockley (38.4 nm), 1/6 <110> stair rod (27 nm), and a few segments of 1/3 <100> Hirth. The dislocations for the (111) orientation were mostly 1/6 <112> Shockley (60 nm), 1/6 <110> Stair-rod (48.22 nm), and 1/3 <100> Hirth (16 nm). Note that the Hirth dislocation can result from reactions between Shockley dislocations as $1/6[\bar{1}21] + 1/6[\bar{1}2\bar{1}] = 1/3[\bar{1}00]$, and the Frank dislocation can result from reactions of Stair-rod and Shockley, e.g., $1/6[011] + 1/6[211] = 1/3[111]$. Hirth dislocations are also known as Hirth locks[37] and Frank dislocations are known as Lomer–Cottrell (LC) locks.[38] These were largely the mechanisms that contributed to the observed plasticity and allied mechanisms observed during HEA nanoscratching during the MD simulations.

The FCC structure has 12 non-equivalent partial dislocation slip systems $\langle 110\rangle/2\text{-}\{111\}$. However, not all of these slip systems are operative during scratching. Based on tensor rotation, we can convert the applied shear (scratching) stress to each of the slip systems. The slip systems with the maximum conversion factors (analogous to the Schmid factor) are operative. We found that the (010) scratching has eight most likely operative slip systems $[101]/2\text{-}(\bar{1}11)$, $[0\bar{1}1]/2\text{-}(\bar{1}11)$, $[101]/2\text{-}(11\bar{1})$, $[011]/2\text{-}(11\bar{1})$, $[011]/2\text{-}(\bar{1}1\bar{1})$, $[10\bar{1}]/2\text{-}(\bar{1}1\bar{1})$, $[0\bar{1}1]/2\text{-}(111)$, $[\bar{1}01]/2\text{-}(111)$ with a conversion factor of 0.41, the $(\bar{1}10)$ scratching has four most likely operative slip systems $[110]/2\text{-}(1\bar{1}1)$, $[1\bar{1}0]/2\text{-}(11\bar{1})$, $[110]/2\text{-}(\bar{1}1\bar{1})$, $[1\bar{1}0]/2\text{-}(111)$ with a conversion factor of 0.82, and the (111) scratching has one most likely operative slip systems $[1\bar{1}0]/2\text{-}(111)$ with a conversion factor 1.00, two second likely operative slip systems $[110]/2\text{-}(\bar{1}11)$, $[110]/2\text{-}(1\bar{1}1)$ with a conversion factor of 0.87, and four third most likely operative slip systems $[101]/2\text{-}(1\bar{1}\bar{1})$, $[011]/2\text{-}(\bar{1}1\bar{1})$, $[0\bar{1}1]/2\text{-}(111)$, $[\bar{1}01]/2\text{-}(111)$ with a conversion factor of 0.50. Note that during the (010) scratching, every slip vector is activated on two slip planes, for instance, the $[101]/2$ vector is activated on the $(\bar{1}11)$ and $(11\bar{1})$ planes in the $[101]/2\text{-}(\bar{1}11)$ and $[101]/2\text{-}(11\bar{1})$ slip systems. This feature is not present on the other two scratching surfaces. As a result, the dislocation morphology observed in Fig. 15(a) for the (010) scratching looks different from Figs. 15(b) and 15(c) for the (110) and (111) scratching planes.

IV. CONCLUSIONS

This paper reports the mechanical properties of a novel high-entropy alloy ($Ni_{25}Cu_{18.75}Fe_{25}Co_{25}Al_{6.25}$) using nano-scratching experiments and MD simulations. This new alloy was synthesized for the first time and was found to reside in the FCC structure.

1. A novel mechanism of cyclic drop in the tensile test of the HEA nanowire was seen from the MD simulations. It was noticed that as soon as the HEA nanowire starts to deform, an intrinsic stacking fault emits from the surface of the wire, traveling at an angle inside the wire until reaching the other end of the wire. Emission of these intrinsic stacking faults relieves the stress intermittently, which revealed a unique insight into the deformation of HEA nanowires in contrast to other FCC metal nanowires.
2. The generalized stacking fault energy (GSFE) curve obtained for HEA on the Shuffle set showed the unstable stacking fault energy (γ_{us}) as 0.02 ev/Å^2 and intrinsic stacking fault energy γ_{isf} of 0.005 eV/Å^2. The corresponding slope of GSFE with respect to the displaced atoms indicated that about 4.8 GPa shear stress triggers first instability in the FCC-HEA structure, paving the way for the defect nucleation.
3. During scratching of $Ni_{25}Cu_{18.75}Fe_{25}Co_{25}Al_{6.25}$, several crystal defects were identified, such as {111} free surface atoms, coherent Σ3 grain boundaries, Σ11 faults or tilt boundaries, stacking faults (SF), and the HCP phase with various layer thicknesses. Additionally, Hirth locks and Lomer–Cottrell (LC) locks were also observed. 1/6 <112> Shockley was seen as the longest dislocation governing the plasticity in FCC HEA. Aside from this, 1/2<110> (perfect), 1/6 <110> (stair-rod), 1/3 <100> (Hirth), and 1/3 <111> Frank partials were seen in the sub-surface and pileup portion of the scratched HEA.
4. On comparing the MD simulations with the experiments, the specific cutting energy (work done by the scratching tool in removing a unit volume of material) showed a strong agreement, whereas the kinetic coefficient of friction differed. The observation was not only seen in this work for the FCC-phase high-entropy alloy but was also seen during the AFM scratching of GaAs reported recently. This suggests that specific cutting energy is a more suitable parameter to compare MD simulation with experiments.

5. A strong anisotropy was seen from the MD simulations of tensile and scratching testing on HEA in terms of uniaxial tensile stress, scratch force, kinetic coefficient of friction, pile up, and side flow during scratching. The (111) orientation showed the highest uniaxial stress, while the (100) orientation showed the highest kinetic coefficient of friction, requiring maximum specific cutting energy.

SUPPLEMENTARY MATERIAL

See the supplementary material for the formulas used to generate Fig. 11 from the stress tensor obtained from the MD data.

ACKNOWLEDGMENTS

P.F. acknowledges the financial support from EPSRC Grant No. EP/V055208/1. S.G. acknowledges the financial support provided by the UKRI via Grants No. EP/S036180/1, EP/T001100/1, and EP/T024607/1, feasibility study awards to LSBU from the UKRI National Interdisciplinary Circular Economy Hub (EP/V029746/1) and Transforming the Foundation Industries: A Network+ (EP/V026402/1), the Hubert Curien Partnership award 2022 from the British Council, Transforming the Partnership award from the Royal Academy of Engineering (Grant No. TSP1332), and the Newton Fellowship award from the Royal Society (Grant No. NIF\R1\191571). This work also accessed the Isambard Bristol, UK supercomputing service, via the Resource Allocation Panel (RAP), as well as ARCHER2 resources (Project No. e648).

Sandia National Laboratories is a multi-mission laboratory managed and operated by National Technology and Engineering Solutions of Sandia, LLC, a wholly owned subsidiary of Honeywell International, Inc., for the U.S. Department of Energy's National Nuclear Security Administration (NNSA) under Contract No. DE-NA-0003525.

The views and opinions of the authors expressed herein do not necessarily state or reflect those of the United States Government or any agency thereof. Neither the United States Government nor any agency thereof, nor any of their employees, makes any warranty, expressed or implied, or assumes any legal liability or responsibility for the accuracy, completeness, or usefulness of any information, apparatus, product, or process disclosed, or represents that its use would not infringe privately owned rights.

AUTHOR DECLARATIONS

Conflict of Interest

The authors have no conflicts to disclose.

Author Contributions

P.F. and N.K.K. have made equal contributions to the work.

Pengfei Fan: Investigation (equal); Writing – original draft (equal). **Nirmal Kumar Katiyar**: Formal analysis (equal); Resources (equal); Software (equal); Writing – original draft (equal). **Xiaowang Zhou**: Methodology (lead); Writing – review & editing (equal). **Saurav Goel**: Conceptualization (supporting); Formal analysis (lead); Methodology (lead); Supervision (lead); Writing – review & editing (equal).

DATA AVAILABILITY

The data that support the findings of this study are openly available in the Strathclyde repository at https://doi.org/10.15129/118b0a4f-c5bc-4d92-948b-f64657e5a144.

REFERENCES

[1] J.-W. Yeh *et al.*, "Nanostructured high-entropy alloys with multiple principal elements: Novel alloy design concepts and outcomes," Adv. Eng. Mater. **6**(5), 299–303 (2004).
[2] B. Cantor, I. T. H. Chang, P. Knight, and A. J. B. Vincent, "Microstructural development in equiatomic multicomponent alloys," Mater. Sci. Eng. A **375–377**(1–2), 213–218 (2004).
[3] N. K. Katiyar *et al.*, "Formic acid and methanol electro-oxidation and counter hydrogen production using nano high entropy catalyst," Mater. Today Energy **16**, 100393 (2020).
[4] S. Nellaiappan *et al.*, "High-entropy alloys as catalysts for the CO_2 and CO reduction reactions: Experimental realization," ACS Catal. **10**(6), 3658–3663 (2020).
[5] K. M. B. Urs *et al.*, "Multi-component (Ag–Au–Cu–Pd–Pt) alloy nanoparticle-decorated p-type 2D-molybdenum disulfide (MoS_2) for enhanced hydrogen sensing," Nanoscale **12**(22), 11830–11841 (2020).
[6] W. Y. Ching, S. San, J. Brechtl, R. Sakidja, M. Zhang, and P. K. Liaw, "Fundamental electronic structure and multiatomic bonding in 13 biocompatible high-entropy alloys," npj Comput. Mater. **6**(1), 45 (2020).
[7] Y. Yuan *et al.*, "Formation, structure and properties of biocompatible TiZrHfNbTa high-entropy alloys," Mater. Res. Lett. **7**(6), 225–231 (2019).
[8] N. K. Katiyar, G. Goel, and S. Goel, "Emergence of machine learning in the development of high entropy alloy and their prospects in advanced engineering applications," Emergent Mater. **4**(6), 1635–1648 (2021).
[9] S. Praveen and H. S. Kim, "High-entropy alloys: Potential candidates for high-temperature applications – An overview," Adv. Eng. Mater. **20**(1), 1700645 (2018).
[10] N. Kaushik, A. Meena, and H. S. Mali, "High entropy alloy synthesis, characterisation, manufacturing & potential applications: A review," Mater. Manuf. Process. **37**(10), 1085–1109 (2022).
[11] A. Ayyagari, R. Salloom, S. Muskeri, and S. Mukherjee, "Low activation high entropy alloys for next generation nuclear applications," Materialia **4**, 99–103 (2018).
[12] P. Edalati *et al.*, "Ultrahigh hardness and biocompatibility of high-entropy alloy TiAlFeCoNi processed by high-pressure torsion," Mater. Sci. Eng. C **112**, 110908 (2020).
[13] N. Savage, "High-entropy alloys expand their range," Nature **595**, 7865 (2021).
[14] V. V. Popov *et al.*, "Powder bed fusion additive manufacturing using critical raw materials: A review," Materials **14**(4), 909 (2021).
[15] A. Mir *et al.*, "Challenges and issues in continuum modelling of tribology, wear, cutting and other processes involving high-strain rate plastic deformation of metals," J. Mech. Behav. Biomed. Mater. **130**, 105185 (2022).
[16] Y. X. Ye, C. Z. Liu, H. Wang, and T. G. Nieh, "Friction and wear behavior of a single-phase equiatomic TiZrHfNb high-entropy alloy studied using a nanoscratch technique," Acta Mater **147**, 78–89 (2018).
[17] S. Goel *et al.*, "Horizons of modern molecular dynamics simulation in digitalized solid freeform fabrication with advanced materials," Mater. Today Chem. **18**, 100356 (2020).
[18] N. H. Faisal, R. Ahmed, S. Goel, and Y. Q. Fu, "Influence of test methodology and probe geometry on nanoscale fatigue failure of diamond-like carbon film," Surf. Coatings Technol. **242**, 42–53 (2014).

[19]S. W. Wu *et al.*, "Strong grain-size effect on deformation twinning of an $Al_{0.1}$CoCrFeNi high-entropy alloy," Mater. Res. Lett. **5**(4), 276–283 (2017).
[20]C. Liu, Y. Yang, and Z. Xia, "Deformation mechanism in Al0.1CoCrFeNi Σ3(111)[110] high entropy alloys-molecular dynamics simulations," RSC Adv **10**(46), 27688–27696 (2020).
[21]G. Luo *et al.*, "Microstructural evolution and mechanical properties of FeCoCrNiCu high entropy alloys: A microstructure-based constitutive model and a molecular dynamics simulation study," Appl. Math. Mech. (Engl. Ed.) **42**(8), 1109–1122 (2021).
[22]Z. Wang, J. Li, Q. Fang, B. Liu, and L. Zhang, "Investigation into nano-scratching mechanical response of AlCrCuFeNi high-entropy alloys using atomic simulations," Appl. Surf. Sci. **416**, 470–481 (2017).
[23]D. Utt *et al.*, "The origin of jerky dislocation motion in high-entropy alloys," Nat. Commun. **13**(1), 4777 (2022).
[24]J. Sun *et al.*, "High temperature tensile properties of as-cast and forged CrMnFeCoNi high entropy alloy," Mater. Sci. Eng. A **850**, 143570 (2022).
[25]J. Kumar, A. Linda, M. Sadhasivam, K. G. Pradeep, N. P. Gurao, and K. Biswas, "The effect of Al addition on solid solution strengthening in CoCrFeMnNi: Experiment and modelling," Acta Mater. **238**, 118208 (2022).
[26]J. Kumar, N. Kumar, S. Das, N. P. Gurao, and K. Biswas, "Effect of Al addition on the microstructural evolution of equiatomic CoCrFeMnNi alloy," Trans. Indian Inst. Met. **71**(11), 2749–2758 (2018).
[27]P. Hirel, "Atomsk: A tool for manipulating and converting atomic data files," Comput. Phys. Commun. **197**, 212–219 (2015).
[28]S. Plimpton, "Fast parallel algorithms for short range molecular dynamics," J. Comput. Phys. **117**, 1–19 (1995).
[29]N. Khatri, B. M. Barkachary, B. Muneeswaran, R. Al-Sayegh, X. Luo, and S. Goel, "Surface defects incorporated diamond machining of silicon," Int. J. Extrem. Manuf. **2**(4), 45102 (2020).
[30]P. Fan, S. Goel, X. Luo, and H. M. Upadhyaya, "Atomic-scale friction studies on single-crystal gallium arsenide using atomic force microscope and molecular dynamics simulation," Nanomanuf. Metrol. **5**, 39 (2021).
[31]X. W. Zhou *et al.*, "Atomic scale structure of sputtered metal multilayers," Acta Mater. **49**(19), 4005–4015 (2001).
[32]X. W. Zhou, R. A. Johnson, and H. N. G. Wadley, "Misfit-energy-increasing dislocations in vapor-deposited CoFe/NiFe multilayers," Phys. Rev. B: Condens. Matter Mater. Phys. **69**(14), 144113 (2004).
[33]V. Vítek, "Thermally activated motion of screw dislocations in B.C.C. metals," Phys. Status Solidi **18**(2), 687–701 (1966).
[34]H. Van Swygenhoven, P. M. Derlet, and A. G. Frøseth, "Stacking fault energies and slip in nanocrystalline metals," Nat. Mater. **3**(6), 399–403 (2004).
[35]V. Vítek, "Intrinsic stacking faults in body-centred cubic crystals," Philos. Mag. A **18**(154), 773–786 (1968).
[36]J. R. Rice, "Dislocation nucleation from a crack tip: An analysis based on the Peierls concept," J. Mech. Phys. Solids **40**(2), 239–271 (1992).
[37]T. Paulauskas *et al.*, "Atomic scale study of Lomer–Cottrell and Hirth lock dislocations in CdTe," Microsc. Microanal. **21**(1042), 2087–2088 (2015).
[38]V. Bulatov, F. F. Abraham, L. Kubin, B. Devincre, and S. Yip, "Connecting atomistic and mesoscale simulations of crystal plasticity," Nature **391**(6668), 669–672 (1998).